

Embedding Atomically Dispersed Iron Sites in Nitrogen-Doped Carbon Frameworks-Wrapped Silicon Suboxide for Superior Lithium Storage

Xiaotian Guo, Hengyue Xu, Wenting Li, Yangyi Liu, Yuxin Shi, Qing Li, and Huan Pang*

Silicon suboxide (SiO_x) has attracted widespread interest as Li-ion battery (LIB) anodes. However, its undesirable electronic conductivity and apparent volume effect during cycling impede its practical applications. Herein, sustainable rice husks (RHs)-derived SiO_2 are chosen as a feedstock to design SiO_x /iron-nitrogen co-doped carbon (Fe-N-C) materials. Using a facile electrospray-carbonization strategy, SiO_x nanoparticles (NPs) are encapsulated in the nitrogen-doped carbon (N-C) frameworks decorating atomically dispersed iron sites. Systematic characterizations including high-angle annular dark-field scanning transmission electron microscopy (HAADF-STEM) and X-ray absorption fine structure (XAFS) verify the existence of Fe single atoms and typical coordination environment. Benefiting from its structural and compositional merits, the SiO_x /Fe-N-C anode delivers significantly improved discharge capacity of 799.1 mAh g^{-1} , rate capability, and exceptional durability, compared with pure SiO_2 and SiO_x /N-C, which has been revealed by the density functional theory (DFT) calculations. Additionally, the electrochemical tests and in situ X-ray diffraction (XRD) analysis reveal the oxidation of Li_xSi phase and the storage mechanism. The synthetic strategy is universal for the design and synthesis of metal single atoms/clusters dispersed N-C frameworks encapsulated SiO_x NPs. Meanwhile, this work provides impressive insights into developing various LIB anode materials suffering from inferior conductivity and huge volume fluctuations.

1. Introduction


Recently, nitrogen-doped carbon (N-C) frameworks supported transition metal ($\text{M} = \text{Fe},^{[1,2]} \text{Co},^{[3]} \text{and Ni}^{[4]}$) single atom or cluster catalysts possess good electrochemical properties, because of satisfactory conductivity and electrochemical activity. In addition, metal-nitrogen-carbon (M-N-C) can promote the adsorption/desorption of active sites, manifesting its applications in oxygen reduction reaction or even metal (Zn, Al, and Li)-air batteries.^[5] M-N-C can also be utilized as sulfur hosts of Li-S batteries with desirable capacity and superior cyclability.^[6] The presence of M-N-C with catalytic attribute can significantly relieve the “shuttle effect” of polysulfide produced during cycling, and further accelerate the formation and decomposition of $\text{Li}_2\text{S}/\text{Na}_2\text{S}$ for Li/Na-S batteries.^[7,8] Li-ion batteries (LIBs) are employed as attractive power sources for multifarious energy storage systems.^[9] It is of great significance whether the M-N-C-based anodes with the catalytic effect can enhance the reversibility of electrochemical reactions during lithium storage and reveal the corresponding interaction between Li^+ and M-N-C.^[10]

The alternative silicon suboxide (SiO_x) ($0 < x \leq 2$) anodes have also been widely investigated for LIB applications because of rich abundance of Si, high capacity, easy synthesis, and low cost.^[11,12] Despite above superiorities, the drawbacks such as obvious volume fluctuations and inferior conductivity of SiO_x still lead to undesirable cycle stability and rate performance.^[13] To solve aforementioned problems, a general strategy is to construct SiO_x composites with metal (Cu,^[14] Ni,^[15] Co,^[16] Ag,^[17] etc.) or/and carbon materials, directly bringing about increased electronic conductivity. Besides, electrochemically inert metals can also serve as buffer space for accommodating volume expansion.^[18] Another strategy for relieving volume effect is to construct core-shell, yolk-shell, hollow structures as well as carbon frameworks.^[19] In addition, achieving a balance between decreasing the size of SiO_x as electroactive component and reducing the agglomeration degree of nanostructures can improve its electrochemical activity, reduce the volume strain, and decrease the inter-particle resistance induced by ineffective contact.^[20] Thus, it is of great significance to design nano- SiO_x composites with desirable structures.

X. Guo, W. Li, Y. Liu, Y. Shi, H. Pang
School of Chemistry and Chemical Engineering
Yangzhou University
Yangzhou, Jiangsu 225009, P. R. China
E-mail: panghuan@yzu.edu.cn; huanpangchem@hotmail.com

H. Xu
Institute of Biopharmaceutical and Health Engineering
Tsinghua Shenzhen International Graduate School
Tsinghua University
Shenzhen 518055, P. R. China

Q. Li
Guangling College
Yangzhou University
Yangzhou, Jiangsu 225009, P. R. China

 The ORCID identification number(s) for the author(s) of this article can be found under <https://doi.org/10.1002/advs.202206084>

© 2022 The Authors. Advanced Science published by Wiley-VCH GmbH. This is an open access article under the terms of the Creative Commons Attribution License, which permits use, distribution and reproduction in any medium, provided the original work is properly cited.

DOI: 10.1002/advs.202206084

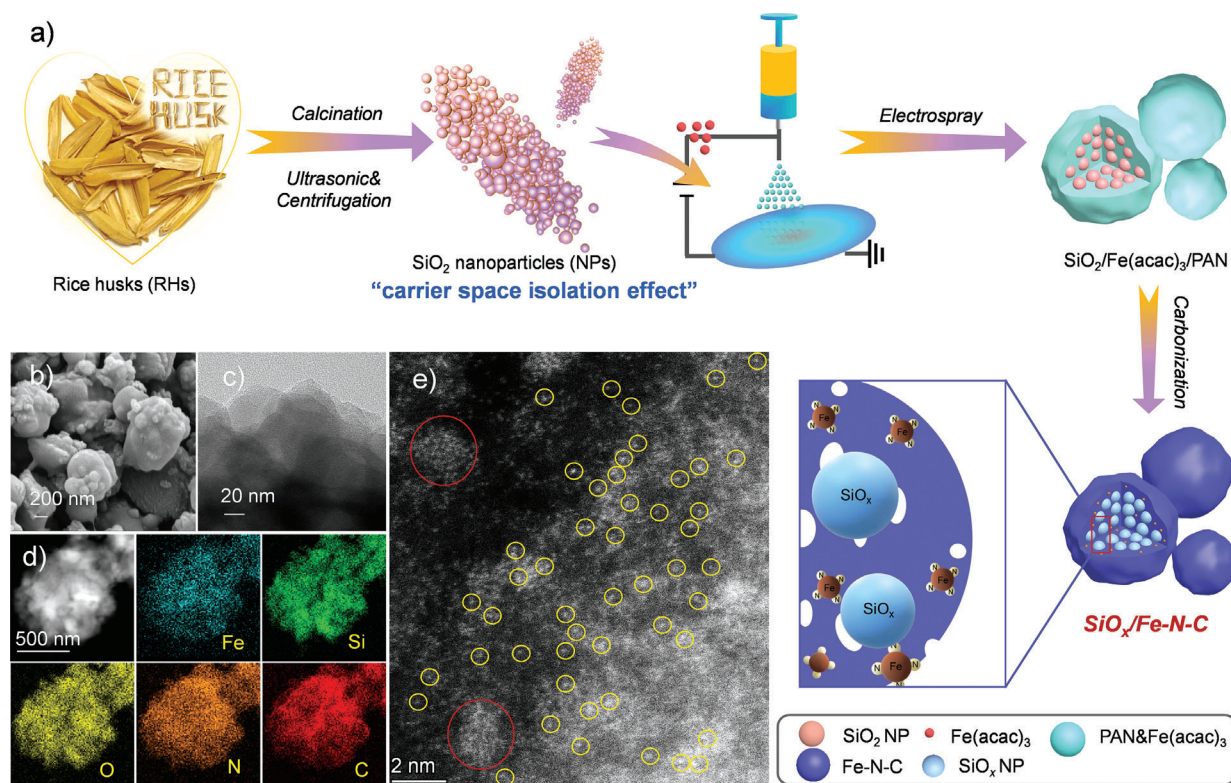


Figure 1. a) Schematic illustration of the fabrication of $\text{SiO}_x/\text{Fe-N-C}$; b,c) Scanning electron microscopy (SEM) and transmission electron microscope (TEM) images of $\text{SiO}_x/\text{Fe-N-C}$; d) Energy dispersive spectrometer (EDS)-mapping result and e) Aberration-corrected HAADF-STEM result of the as-synthesized $\text{SiO}_x/\text{Fe-N-C}$ product.

In terms of Si sources, biomass resources (bamboo leaves,^[15] reed leaves,^[21] rice husks (RHs),^[22] etc.) can provide sustainable and abundant SiO_2 precursors for further synthesis of SiO_x -based materials. Herein, we utilized rice husks as SiO_2 precursors and adopted a combined strategy of electrospay-carbonization processes to prepare $\text{SiO}_x/\text{Fe-N-C}$ materials. SiO_x NPs with good dispersion were encapsulated in Fe single atoms decorated N-C frameworks. The aberration-corrected high-angle annular dark-field scanning transmission electron microscopy (HAADF-STEM) and X-ray absorption fine structure (XAFS) tests verified the presence of Fe single atoms and Fe-N coordination mode. When $\text{SiO}_x/\text{Fe-N-C}$ was used as LIB anodes, it exhibited high discharge capacities of 799.1 mAh g^{-1} at the 100th cycle and 173.7 mAh g^{-1} at the 5000th cycle even at 5 A g^{-1} . By combining density functional theory (DFT) calculations, in situ X-ray diffraction (XRD) technique and ex situ morphology and structural characterizations, we concluded the reasons for significantly improved performance of the $\text{SiO}_x/\text{Fe-N-C}$ anode and revealed the oxidation of Li_xSi phase as well as the storage mechanism. Its unique structural and compositional advantages rendered efficient active sites for lithium storage, promoted its electrochemical reversibility with the catalytic attribute of Fe single atoms, and buffered its volume fluctuations of SiO_x NPs. The rational syntheses of $\text{SiO}_x/\text{M-N-C}$ ($\text{M} = \text{Fe, Co, Ni}$) demonstrated that such strategy could be extended for fabricating other SiO_x -based composites or M-N-C materials. In view of the effect of M-N-C on lithium storage, these materials are expected for diverse applications.

2. Results and Discussion

The whole synthetic procedure for preparing the $\text{SiO}_x/\text{Fe-N-C}$ product is presented in **Figure 1a**. RHs was initially washed and acid treated for subsequent calcination to obtain SiO_2 powder, of which the powder was mainly composed of biomass skeleton and SiO_2 NPs (Figure S1a,b, Supporting Information). Furthermore, SiO_2 NPs with average particle sizes of 20–80 nm can be easily separated with the assistance of ultrasonic and centrifugal processes (Figure S1c,d, Supporting Information), showing a lower aggregation degree compared with other nanosized SiO_2 .^[22] This is crucial for preparing carbon coated SiO_x composites. Afterward, the precursor solution containing polyacrylonitrile (PAN), SiO_2 NPs, and $\text{Fe}(\text{acac})_3$ was used to produce $\text{SiO}_x/\text{Fe-N-C}$ microspheres through the electrospay-carbonization strategy. For comparison, the precursor solution without adding $\text{Fe}(\text{acac})_3$ was denoted as $\text{SiO}_x/\text{N-C}$.

The as-synthesized $\text{SiO}_x/\text{Fe-N-C}$ composites have an irregular spherical morphology with average sizes of $\approx 0.5\text{--}1 \mu\text{m}$ (Figure 1b). Similarly, the $\text{SiO}_x/\text{N-C}$ sample exhibited a similar micro-spherical morphology and size with $\text{SiO}_x/\text{Fe-N-C}$ (Figure S2, Supporting Information). Furthermore, SiO_x NPs were enwrapped by the micro-spherical framework, and no obvious metallic Fe NPs were detected from its edge of spherical framework (Figure 1c). Moreover, the high-resolution transmission electron microscopy (HRTEM) and selected area electron diffraction (SAED) images demonstrated that no obvious crystal lattice and diffraction fringes could be observed (Figure S3, Supporting

Information), indicating that the components of SiO_x and carbon were both amorphous.^[23] Theoretically, the product synthesized by the electrospray-carbonization strategy should contain Fe, Si, O, C, and N elements, as revealed by the energy dispersive spectrometer (EDS)-mapping images (Figure 1d). The Fe element was homogeneously distributed in $\text{SiO}_x/\text{Fe-N-C}$. Therefore, the existing form of Fe species is of great significance to be investigated by the HAADF-STEM technique. For $\text{SiO}_x/\text{Fe-N-C}$, Fe single atoms (yellow circles) and a small number of atomic clusters (red circles) could be detected rather than Fe NPs (Figure 1e). Fe single atoms and clusters mainly appeared near the edge of the microspheres and around SiO_x NPs, respectively. The mass loadings of Fe (≈ 6 wt%), N-C (≈ 43 wt%), and SiO_x (≈ 51 wt%) in $\text{SiO}_x/\text{Fe-N-C}$ were determined by a combination of thermogravimetric analysis (TGA) (Figure S4, Supporting Information), inductively coupled plasma optical emission spectroscopy (ICP-OES), and X-ray photoelectron spectroscopy (XPS) results (Table S1, Supporting Information). The synthetic strategy is of great significance for obtaining relatively high mass loading of metal single atoms. The synthetic basis for introducing Fe single atoms can be ascribed to the carrier space isolation effect of SiO_2 or SiO_x NPs.^[24] Apart from reducing the aggregation of Fe salts, the presence of N-C promoted the formation of Fe-N active sites at the molecular level after carbonization,^[25] which was subsequently proved by the XAFS characterization.

Meanwhile, since the metal salts were almost dissolved in the precursor solution, the formation of Fe clusters in N-C was inevitable due to the inside distribution of SiO_x NPs.^[26] Theoretically, the catalytic activity of atomic and clusters is much higher than that of Fe NPs. Meanwhile, we have tried to reduce the formation of Fe clusters by increasing the concentration of SiO_x NPs. However, it is difficult to obtain the electrospray products with good carbon coating since the concentration of PAN is very low, which could lead to serious agglomeration of SiO_x NPs and poor electrochemical activity for lithium storage. Herein, we have proved that Fe element in $\text{SiO}_x/\text{Fe-N-C}$ mainly existed as Fe single atoms rather than atomic clusters around SiO_x as described above. Therefore, it is focused on investigating whether Fe single atoms have an elevating effect on the reversibility of SiO_x during cycling, and the DFT calculations involving the influence of Fe single atoms.

To analyze the influence of carbonization temperature on the detailed Fe species, the basic morphology characterization of the C1 and C2 samples were conducted. The overall spherical morphology of C1 and C2 was similar with that of $\text{SiO}_x/\text{Fe-N-C}$. No obvious Fe NPs displayed in the TEM, HRTEM, and SAED images could be found (Figure S5a-e, Supporting Information), and Fe element was evenly distributed in the EDS-mapping results (Figure S5f, Supporting Information). This result was similar with that of $\text{SiO}_x/\text{Fe-N-C}$, which implied that the Fe element was successfully doped in the N-C framework. Instead, when the carbonization temperature was determined to be 750 °C, Fe NPs were strongly distinguished by the TEM, HRTEM, and SAED images of the C2 sample (Figure S6a-e, Supporting Information). The size of the Fe NPs was obviously over 20 nm, and the distribution of Fe element could confirm that the Fe species of C2 were metallic NPs (Figure S6f, Supporting Information), which was also revealed by the XRD curve (Figure S6g, Supporting Information). In short, the Fe species changed from

single atoms/clusters to NPs when elevating the carbonization temperature, showing an apparent agglomeration tendency of atoms. When choosing suitable carbonization temperature, the N-C species decomposed from PAN could subsequently bind with Fe atoms to generate Fe-N_x moieties, inhibiting Fe atoms from serious aggregation.^[27,28]

XRD patterns of the three samples displayed a broad peak located between 20° and 30° (Figure 2a), corresponding to amorphous SiO_2 , SiO_x , and N-C.^[29,30] No obvious signals of Fe and FeO_x were found, excluding the existence of good crystalline component of Fe-containing species. Besides, the Raman spectra also exhibited two typical D-band (1353 cm^{-1}) and G-band (1591 cm^{-1}) for carbon (Figure S7, Supporting Information).^[31] Furthermore, we employed XAFS technique for its detailed analysis of chemical state and corresponding coordination environment of the $\text{SiO}_x/\text{Fe-N-C}$ product. Figure 2b displays the X-ray absorption near edge structure (XANES) spectra of $\text{SiO}_x/\text{Fe-N-C}$ and their reference samples of Fe foil and FePc. The energy absorption threshold of $\text{SiO}_x/\text{Fe-N-C}$ was closer to FePc at the Fe K-edge, indicating that the $\text{Fe}^{\delta+}$ with positive charge was stabilized by N atoms.^[32] In addition, the pre-edge peak of $\text{SiO}_x/\text{Fe-N-C}$ located at about 7114.2 eV was consistent with the representative Fe-N₄ structure.^[33] Figure 2c provides the Fourier transform extended-XAFS (FT-EXAFS) results. For $\text{SiO}_x/\text{Fe-N-C}$, the existence of Fe-N bond (1.48 Å) demonstrated that Fe atoms were primarily coordinated with N atoms rather than other Fe atoms (Fe-Fe bond at about 2.20 Å), which was identical with FePc.^[34] Wavelet transform (WT) can also be employed for the analysis of the Fe K-edge EXAFS oscillations. The WT-EXAFS result of $\text{SiO}_x/\text{Fe-N-C}$ displayed an obvious intensity maximum of $\approx 5.0 \text{ \AA}^{-1}$, which was close to that of FePc and completely distinct from that of reference Fe foil ($\approx 8.0 \text{ \AA}^{-1}$) (Figure 2d-f).^[35] The detailed chemical configuration of Fe was further revealed by the corresponding FT-EXAFS fittings in R and k spaces. As exhibited in Figure 2g,h and Figure S8 (Supporting Information), the average coordination number (4.8) and bond length (1.92 Å) for Fe-N in $\text{SiO}_x/\text{Fe-N-C}$ were found (Table S2, Supporting Information).^[36] Based on the afore-mentioned HAADF-STEM and XAFS results, the Fe single atoms as primary Fe species in $\text{SiO}_x/\text{Fe-N-C}$ and the existence of Fe-N bonds were confirmed.

Additionally, the XPS measurement of $\text{SiO}_x/\text{Fe-N-C}$ was also employed for the analysis of its chemical compositions. All elements were involved in $\text{SiO}_x/\text{Fe-N-C}$ (Figure S9a, Supporting Information). The N 1s spectrum showed that it mainly involved pyridinic (398.6 eV), pyrrolic (400.2 eV), graphitic (401.2 eV) nitrogen, and Fe-N (399.6 eV) species, providing abundant sites for fixing Fe atoms (Figure S9b, Supporting Information).^[37] The Si 2p spectrum could be fitted into the characteristic peaks of Si^{2+} , Si^{3+} , and Si^{4+} (Figure S9c, Supporting Information). Compared to pure SiO_2 (Figure S10, Supporting Information), three different valences of Si could be observed, which was caused by the reduction of N-C on Si^{4+} in SiO_2 at high temperature. Besides, the corresponding O 1s, C 1s, and Fe 2p spectra results were provided in Figure S9d-f (Supporting Information). For comparison, the XPS results of C1 and C2 (Figures S11 and S12, Supporting Information) were consistent with the afore-mentioned TEM and HRTEM results. The $\text{SiO}_x/\text{Fe-N-C}$ sample showed a much smaller specific surface area (35.8 $\text{m}^2 \text{ g}^{-1}$), compared with that of the SiO_2 precursor (193.3 $\text{m}^2 \text{ g}^{-1}$) (Figure 2i). This was attributed

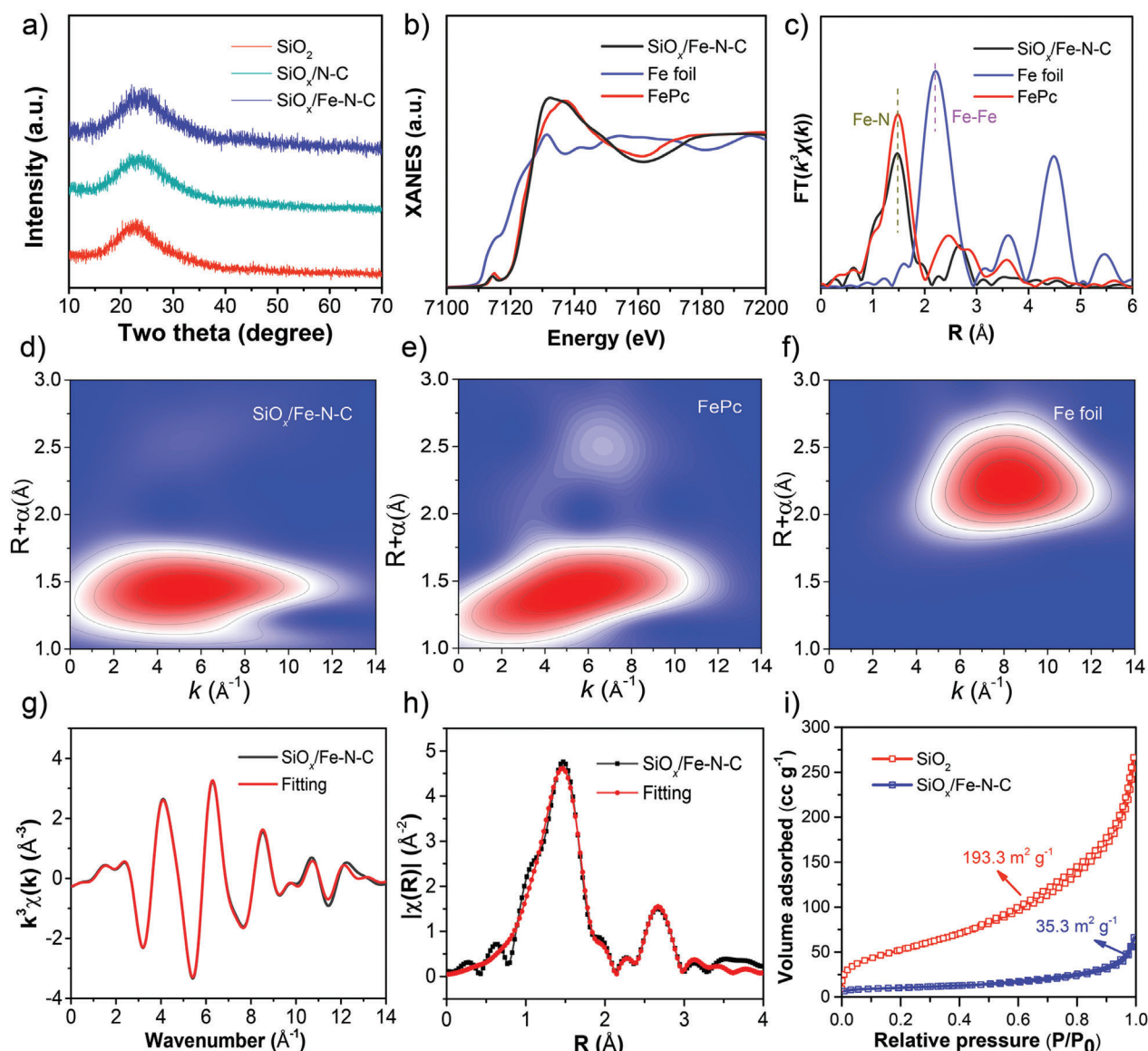


Figure 2. a) XRD curves of pristine SiO_2 , $\text{SiO}_x/\text{N-C}$, and $\text{SiO}_x/\text{Fe-N-C}$. The $\text{SiO}_x/\text{Fe-N-C}$, reference Fe foil and FePc samples. b) XANES results; c) FT-EXAFS results; d–f) WT-EXAFS analysis; g,h) The corresponding EXAFS K-space and R-space fitting curves of $\text{SiO}_x/\text{Fe-N-C}$; i) N_2 absorption–desorption isotherms of the pristine SiO_2 and $\text{SiO}_x/\text{Fe-N-C}$ samples.

to that SiO_x NPs were compactly wrapped by Fe–N–C, of which the frameworks could effectively reduce the side reactions resulting from its direct exposure of SiO_x NPs and thus promoted capacity and cyclability.^[38] Meanwhile, $\text{SiO}_x/\text{Fe-N-C}$ had a smaller pore volume ($0.1 \text{ cm}^3 \text{ g}^{-1}$) and a broad pore size distribution (2–10 nm) (Figure S13, Supporting Information), which ensured reversible intercalation and deintercalation of Li^+ in $\text{SiO}_x/\text{Fe-N-C}$.^[23]

Based on above morphology and structural characterizations of $\text{SiO}_x/\text{Fe-N-C}$, the synthetic strategy could also be extended for obtaining $\text{SiO}_x/\text{Co-N-C}$ and $\text{SiO}_x/\text{Ni-N-C}$. The products synthesized by electrospray-carbonization strategy showed similar spherical morphology with diameters of 0.5–2 μm (Figure 3a–d). The HAADF-STEM image of $\text{SiO}_x/\text{Co-N-C}$ displayed that the Co species mainly exist as Co single atoms (yellow circle)

and small amounts of Co clusters (red circle) appeared near the edge of the microspheres (Figure 3e,f). For $\text{SiO}_x/\text{Co-N-C}$, the apparent pre-edge peak at $\approx 7109.9 \text{ eV}$ could be detected by the XANES result, suggesting a square-planar Co-N_4 structure (Figure 3i). Co atoms were coordinated with N atoms rather than other Co atoms, which were identical with CoPc and consistent with the dominant presence of Co singles atoms (Figure 3j). Unlike $\text{SiO}_x/\text{Co-N-C}$, large amounts of Ni clusters (red circle) of $\approx 2 \text{ nm}$ in size, and small amounts of Ni single atoms (yellow circle) were observed (Figure 3g,h). The corresponding XANES and FT-EXAFS analysis confirmed its composition and obvious existence of Ni clusters (Figure 3k,l). Overall, the electrospray-carbonization method was reasonable and universal for the designing $\text{SiO}_x/\text{M-N-C}$ or M-N-C materials, which could be further applied in various rechargeable batteries or electrocatalysts.

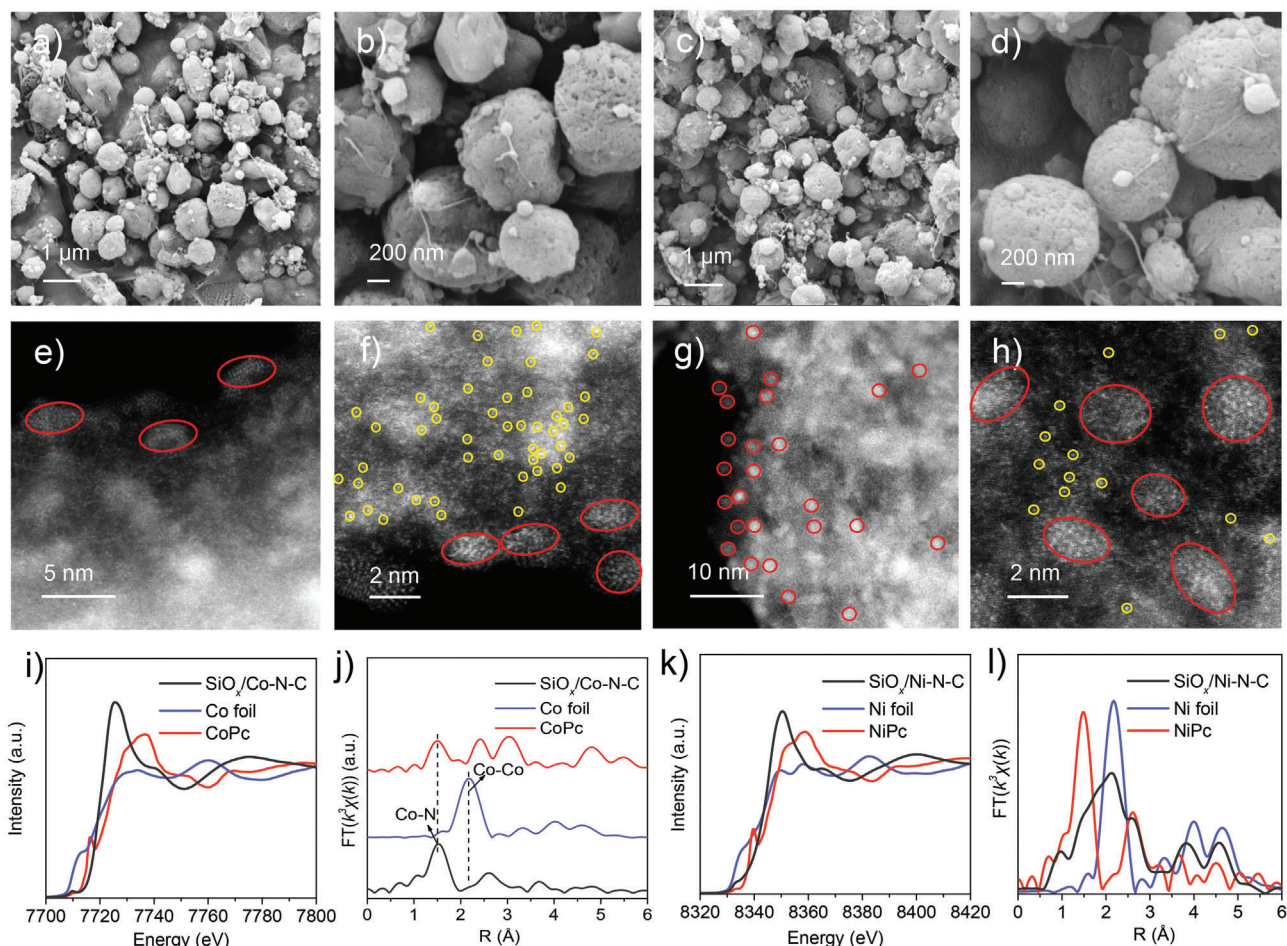


Figure 3. Universal synthesis of $\text{SiO}_x/\text{Co-N-C}$ and $\text{SiO}_x/\text{Ni-N-C}$. a,b) SEM images of $\text{SiO}_x/\text{Co-N-C}$; c,d) SEM images of $\text{SiO}_x/\text{Ni-N-C}$; e,f) HAADF-STEM images of $\text{SiO}_x/\text{Co-N-C}$; g,h) HAADF-STEM images of $\text{SiO}_x/\text{Ni-N-C}$; i,j) XANES and FT-EXAFS analysis of $\text{SiO}_x/\text{Co-N-C}$, reference Co foil and CoPc; k,l) XANES and FT-EXAFS results of the $\text{SiO}_x/\text{Ni-N-C}$ sample, reference Ni foil and NiPc.

To measure the lithium storage performance and of pure SiO_2 , $\text{SiO}_x/\text{N-C}$, and $\text{SiO}_x/\text{Fe-N-C}$ materials as LIB anodes and the effect of different compositions, the representative 2032 coin-type cells based on lithium foil as the counter electrode were assembled. **Figure 4a,b** and **Figure S14a** (Supporting Information) display the above three cyclic voltammogram (CV) curves, respectively. Taking $\text{SiO}_x/\text{Fe-N-C}$ as an example, the reduction peaks at 1.43 and 0.57 V were detected during the 1st cathodic process and disappeared in the later cycles, which were assigned by the decomposition of electrolyte and the generation of the solid electrolyte interface (SEI) film.^[39] A remaining steep peak of ≈ 0.01 V resulted from its alloying reaction of Si and Li^+ for the generation of Li_xSi .^[40] Notably, in the 1st anodic curve, the existence of 0.47 V represented the dissociation process of Li_xSi .^[41,42] A broad anodic peak (≈ 0.92 V) corresponded to the Li^+ extraction of Li-containing components ($\text{Li}_2\text{Si}_2\text{O}_5$, LiC_x).^[43,44] The remaining 2nd and 3rd cycles with no distinct changes demonstrated its superb reversibility. In general, compared with the anodic scans of $\text{SiO}_x/\text{M-N-C}$ ($\text{M} = \text{Fe}, \text{Co}, \text{Ni}$), the dissociation peak of Li_xSi could not be directly detected in that of $\text{SiO}_x/\text{N-C}$ (**Figure S14b,c**, Supporting Information). Moreover, the $\text{SiO}_x/\text{N-C}$ sample displayed a wider range, higher potential and lower current intensity

of the dissociation peak (≈ 1.2 V). Above results could be related to the introduction of metal single atoms with catalytic attribute into the N-C frameworks, promoting the dissociation of amorphous Li_xSi alloy and the utilization of Si for boosted electrochemical reversibility.^[10,45]

Figure S15 (Supporting Information) shows the classic discharge/charge curves of the SiO_2 , $\text{SiO}_x/\text{N-C}$, and $\text{SiO}_x/\text{Fe-N-C}$ anodes at 100 mA g^{-1} . The $\text{SiO}_x/\text{Fe-N-C}$ anode delivered 1st discharge/charge capacities of $1226.9/758.3 \text{ mAh g}^{-1}$ along with a 61.8% coulombic efficiency. Different discharge capacities of 821.3, 820.4, and 821.9 mAh g^{-1} were achieved for the optimized $\text{SiO}_x/\text{Fe-N-C}$ anode after 2, 20, and 50 cycles, respectively. $\text{SiO}_x/\text{Fe-N-C}$ exhibited much superior capacities than SiO_2 and $\text{SiO}_x/\text{N-C}$. Meanwhile, the discharge capacities of 78.6, 515.4, and 799.1 mAh g^{-1} were achieved at the 100th cycle for pure SiO_2 , $\text{SiO}_x/\text{N-C}$, and $\text{SiO}_x/\text{Fe-N-C}$, respectively (**Figure 4c**). Only a decrease of capacity (22.2 mAh g^{-1}) and a 2.7% capacity decay from the 2nd to the 100th cycle was retained for $\text{SiO}_x/\text{Fe-N-C}$, illustrating a critical role of the SEI film during cycling on maintaining the discharge capacities.^[13] **Figure 4d** and **Figure S16** (Supporting Information) show the rate performance. The $\text{SiO}_x/\text{Fe-N-C}$ product delivered reversible discharge capacities

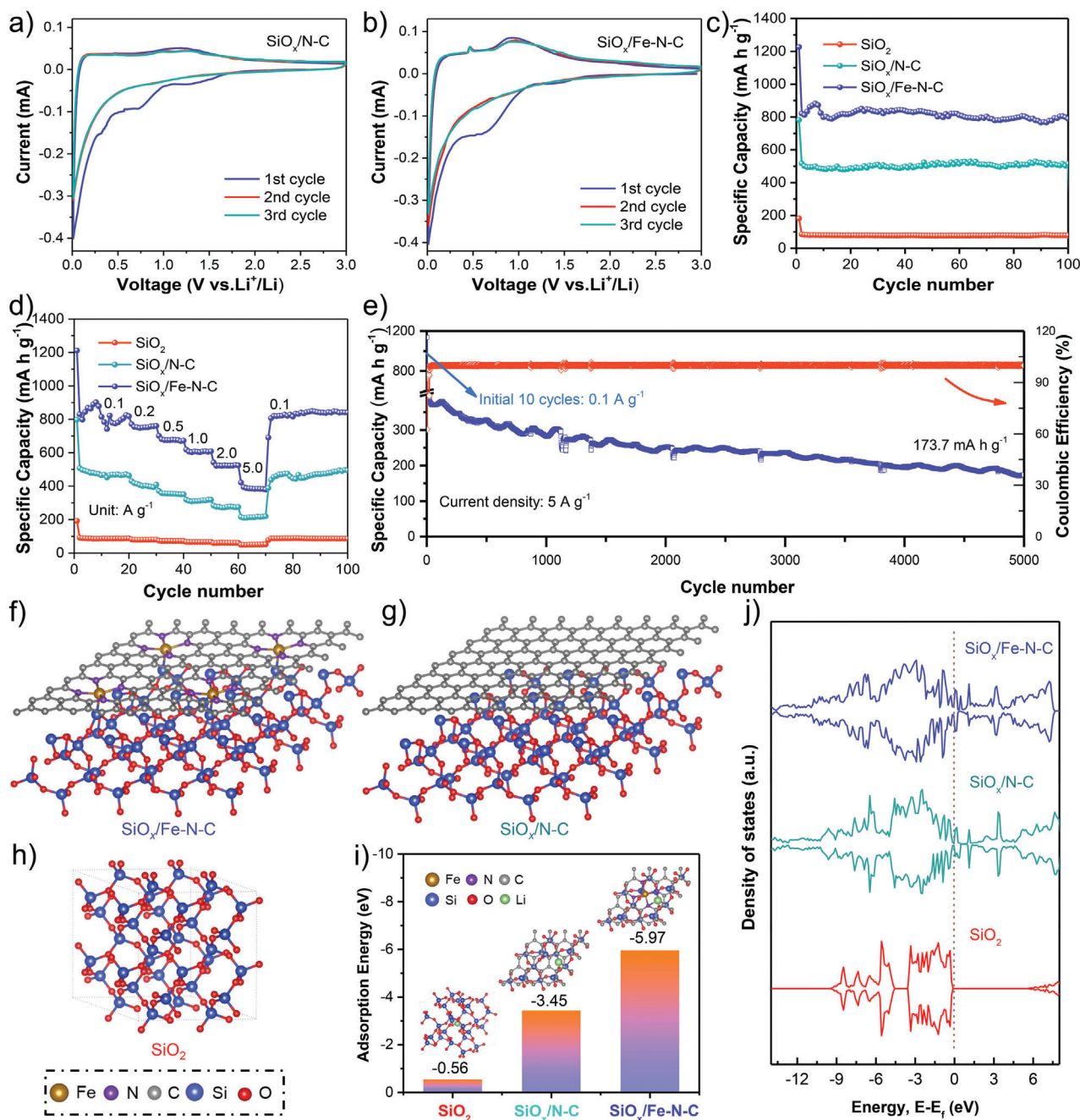


Figure 4. a,b) CV curves of SiO_x/N-C and SiO_x/Fe-N-C, respectively; c) Cycling stability of the SiO₂, SiO_x/N-C and SiO_x/Fe-N-C samples at 100 mA g⁻¹; d) Rate performance of SiO₂, SiO_x/N-C, and SiO_x/Fe-N-C; e) Long-term cyclability of SiO_x/Fe-N-C at 5 A g⁻¹. DFT calculations of the SiO_x/Fe-N-C, SiO_x/N-C, and α-SiO₂ samples. f-h) The calculated geometry configurations; i) The calculated Li adsorption energy; j) The DOS results.

of 801.4, 750.7, 677.8, 613.2, 532.0, and 386.2 mAh g⁻¹ at 0.1, 0.2, 0.5, 1.0, 2.0, and 5.0 A g⁻¹, respectively, and achieved 826.7 mAh g⁻¹ when its current recovered to 0.1 A g⁻¹. Compared with the pure SiO₂ and SiO_x/N-C samples, the rate capability of SiO_x/Fe-N-C was significantly enhanced, demonstrating that the conductivity was promoted and the result was later proved by the density of states (DOS) calculation. It was noted that the superior lithium storage performance of the as-obtained SiO_x/Fe-N-C composite was highly comparable among those of

various SiO_x-based anodes (Figure S17, Table S3, Supporting Information).

The electrochemical impedance spectroscopy (EIS) measurements were also provided for investigating the effect of Fe-N-C on improved rate capability before cycling. In the EIS curves of the three samples, the typical high-frequency semicircles and the low-frequency inclined line can reveal the charge-transfer resistance (R_{ct}) and the diffusion process of Li⁺, respectively (Figure S18, Supporting Information). SiO_x/Fe-N-C had a much

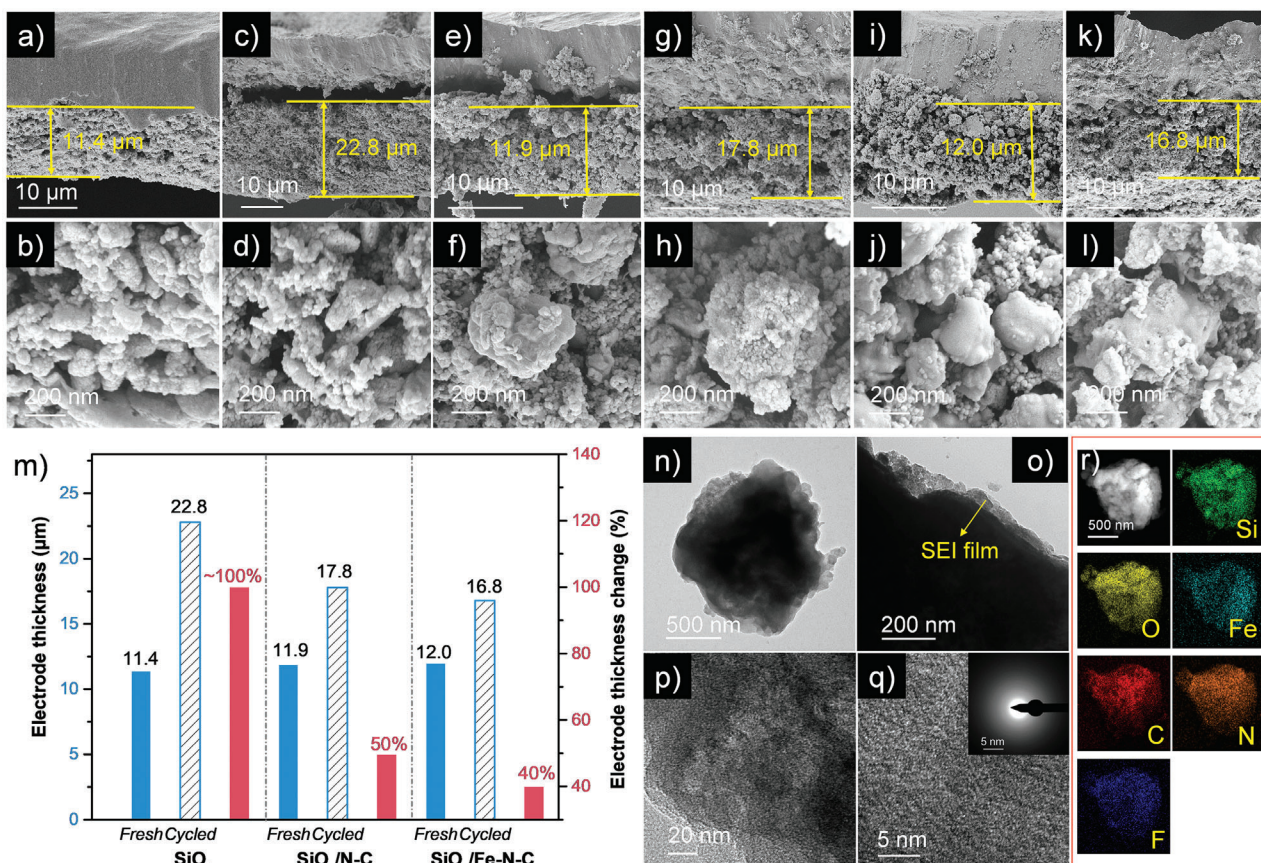


Figure 5. SEM images. a, b) SiO_2 before cycling; c, d) SiO_2 after cycling; e, f) $\text{SiO}_x/\text{N-C}$ before cycling; g, h) $\text{SiO}_x/\text{N-C}$ after cycling; i, j) $\text{SiO}_x/\text{Fe-N-C}$ before cycling; k, l) $\text{SiO}_x/\text{Fe-N-C}$ after cycling; m) Bar chart of the electrode thickness and corresponding change rate for the fresh and cycled SiO_2 , $\text{SiO}_x/\text{N-C}$, and $\text{SiO}_x/\text{Fe-N-C}$ anodes; n–p) TEM images of the cycled $\text{SiO}_x/\text{Fe-N-C}$ sample; q) HRTEM and inserted SAED images of the $\text{SiO}_x/\text{Fe-N-C}$ anode after cycling; r) EDS-mapping patterns of $\text{SiO}_x/\text{Fe-N-C}$ after cycling.

smaller R_{ct} value (72.1Ω) than $\text{SiO}_x/\text{N-C}$ (118.2Ω) and fresh SiO_2 (165.8Ω), revealing that introducing Fe-N-C was more efficient for enhancing the conductivity of SiO_x .^[46] Besides, the optimized $\text{SiO}_x/\text{Fe-N-C}$ sample displayed superior long-term cycle performance with a discharge capacity of 173.7 mAh g^{-1} after 5000 cycles at 5 A g^{-1} , as indicated in Figure 4e.

At the same time, to assess the lithium adsorption abilities of the optimized $\text{SiO}_x/\text{Fe-N-C}$ product, the first-principles DFT calculations of adsorption energy for pristine SiO_2 , $\text{SiO}_x/\text{N-C}$, and $\text{SiO}_x/\text{Fe-N-C}$ was performed. Notably, the effect of Fe single atoms on lithium storage performance was mainly considered. The valence of Si element in $\text{SiO}_x/\text{N-C}$ or the optimized $\text{SiO}_x/\text{Fe-N-C}$ sample was close to the valence of Si in SiO_2 . Thus, according to the ever-reported references, the three models were constructed (Figure 4f–h). As a result, the lithium adsorption energies were determined to be -0.56 , -3.45 , and -5.97 eV for the pure SiO_2 , $\text{SiO}_x/\text{N-C}$, and $\text{SiO}_x/\text{Fe-N-C}$ products, respectively (Figure 4i). $\text{SiO}_x/\text{Fe-N-C}$ possessed the strongest adsorption ability, which was consistent with the highest discharge capacity.^[47,48] In addition, the DOS calculation was employed to investigate the electrical conductivity (Figure 4j). The introduction of Fe-N-C significantly improved the conductivity of SiO_x resulting from the largest density difference at Fermi level.^[1] Therefore, Fe-N-C can exhibit the greatest poten-

tial in achieving the best capacity and rate capability for lithium storage.

To study the charge storage processes of $\text{SiO}_x/\text{Fe-N-C}$, the CV tests were carried out at diverse rates of $0.2\text{--}1.0 \text{ mV s}^{-1}$ (Figure S19a, Supporting Information). Generally, their logarithmic values of the scan rates (v) and the peak currents (i) conformed to the equations ($i = av^b$; $\log i = b \log v + \log a$). Among a and b acting as the regulable parameters, the b-values of 0.5 and 1.0 can stand for an ideal diffusion/pseudocapacitive-controlled processes, respectively.^[49] The b-values of 0.68 and 0.81 were obtained for $\text{SiO}_x/\text{Fe-N-C}$ (Figure S19b, Supporting Information), revealing that its charge storage process was determined by diffusion- and pseudocapacitive-controlled behaviors.^[50] In addition, the pseudocapacitive contributions at varied rates for $\text{SiO}_x/\text{Fe-N-C}$ were displayed and their values of 61.3%, 65.9%, 72.8%, 75.3%, and 77.2% were achieved, respectively (Figure S20a–f, Table S4, Supporting Information). The $\text{SiO}_x/\text{Fe-N-C}$ anode showed much higher values than those of non-metal doped $\text{SiO}_x/\text{N-C}$ (Figures S21 and S22, Supporting Information), indicating Fe-doping promoted its electrochemical reaction and storage reversibility.

Apart from basal electrochemical tests, the structural stability of $\text{SiO}_x/\text{Fe-N-C}$ was further analyzed by the SEM characterizations. The results of comparable pure SiO_2 and $\text{SiO}_x/\text{N-C}$ were

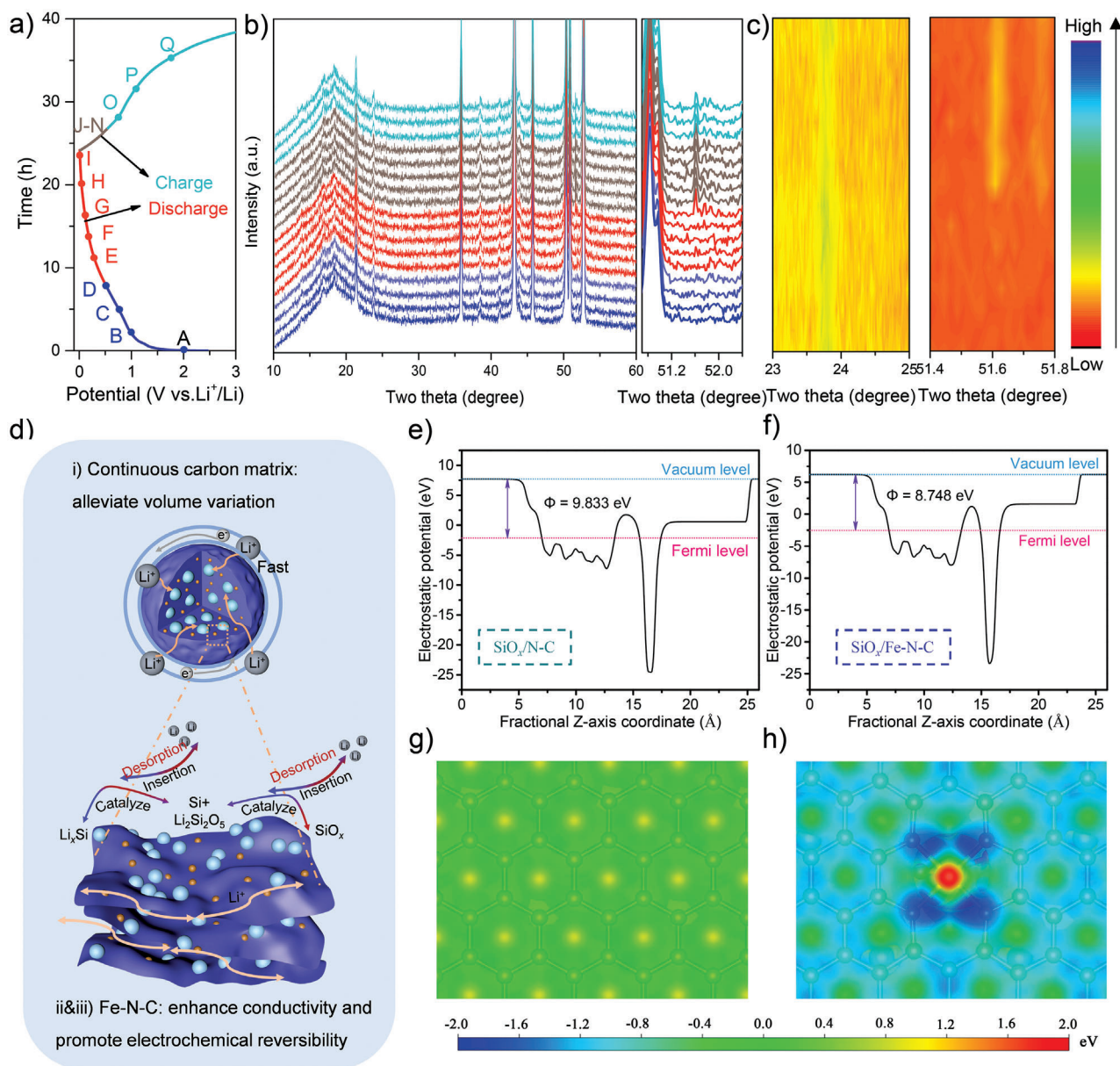


Figure 6. a,b) In situ XRD curves under different voltages and the corresponding charge/discharge curves of $\text{SiO}_x/\text{Fe-N-C}$; c) The corresponding contour plots of $\text{SiO}_x/\text{Fe-N-C}$; d) Schematic illustration of the reversible conversion-alloy reaction for boosted lithium storage performance of $\text{SiO}_x/\text{Fe-N-C}$ during the discharging/charging processes; e,f) The work functions for $\text{SiO}_x/\text{N-C}$ and $\text{SiO}_x/\text{Fe-N-C}$, respectively; The calculated electron-density isosurface for g) $\text{SiO}_x/\text{N-C}$ and h) $\text{SiO}_x/\text{Fe-N-C}$, respectively. The electron-density isosurface was plotted at 0.01 e bohr^{-3} . The color bar represented the electrostatic potential scale.

also given. The cross-sectional thickness of the pure SiO_2 anode increased from 11.4 to 22.8 μm after cycling, and the agglomerated particle structure were obviously damaged (Figure 5a–d).^[51] By contrast, the thickness of $\text{SiO}_x/\text{Fe-N-C}$ increased from 12.0 to 16.8 μm , and the micro-spherical structure could be well observed after 100 cycles (Figure 5e–h), of which the thickness change was smaller than that of $\text{SiO}_x/\text{N-C}$ (Figure 5i–m). Figure 5n–q demonstrates the presence of stable SEI film and its good structural integrity of the cycled $\text{SiO}_x/\text{Fe-N-C}$ anode.^[52] Moreover, the amorphous properties of $\text{SiO}_x/\text{Fe-N-C}$ after cycling were not changed and no obvious Fe NPs could be detected. The EDS-

mapping result also showed the existence of F element, resulting from LiF as a component of the indispensable SEI film (Figure 5r). Above results illustrated that Fe-N-C efficiently relieved the volume fluctuations upon cycling and maintained its structural stability.

More importantly, to study its lithium storage mechanism of the as-synthesized $\text{SiO}_x/\text{Fe-N-C}$ anode, the in situ XRD measurements were performed. The XRD curves under different voltages and the corresponding charge/discharge curves (0.01–3.0 V) are displayed in Figure 6a,b, respectively. As a result, the diffraction peaks involved the typical signals of Be foil (45.9°,

50.9°, 52.8°), BeO (38.6°, 41.3°, 43.8°), Li foil (35.9°, 51.9°), and Cu foil (43.3°), which were not participated in the electrochemical reaction upon cycling.^[53] The corresponding contour plots are displayed in Figure 6c. It is notable that the peak at 23.8° in the contour plot was related with the formation of Li_xSi and the peak at 51.7° could be assigned to the formation of Si, mainly resulting from the dissociation of amorphous Li_xSi , which were consistent with the CV curves.^[54–56] The signal of Si became weak but still existed when the voltage was charged to 3.0 V. This is because the generation of Si during the first discharge process cannot completely convert into SiO_x ($\text{SiO}_x + 2x\text{Li}^+ + 2xe^- \rightarrow x\text{Li}_2\text{O} + \text{Si}$; $\text{SiO}_x + x\text{Li}^+ + xe^- \rightarrow 0.25x\text{Li}_4\text{SiO}_4 + (1-0.25x)\text{Si}$; $\text{SiO}_x + 0.4x\text{Li}^+ + 0.4xe^- \rightarrow 0.2x\text{Li}_2\text{Si}_2\text{O}_5 + (1-0.4x)\text{Si}$; $\text{Si} + x\text{Li}^+ + xe^- \leftrightarrow \text{Li}_x\text{Si}$ ($x \leq 4.4$).^[57] Normally, partial $\text{Li}_2\text{Si}_2\text{O}_5$ can transform into SiO_x . Thus, the reversible formation and dissociation of Li_xSi could improve the utilization of Si and promote the electrochemical reversibility.^[45] Furthermore, the most probable conversion-alloy reaction mechanism of SiO_x in $\text{SiO}_x/\text{Fe-N-C}$ composite was confirmed, as schematically indicated in Figure 6d.

In addition, the work function is close related to the electrochemical properties of its material surface and can reflect the relative difficulty level of the electron escaping from the surface. The calculations of the work functions for the $\text{SiO}_x/\text{N-C}$ and as-obtained $\text{SiO}_x/\text{Fe-N-C}$ samples were performed and their values of 9.833 and 8.748 eV were determined (Figure 6e,f). The lower value of the work function for $\text{SiO}_x/\text{Fe-N-C}$ was beneficial for promoting its electron transfer and catalyze the electrochemical reactions such as the dissociation/formation of amorphous Li_xSi .^[58,59] Moreover, the electron-density isosurface of $\text{SiO}_x/\text{Fe-N-C}$ also verified higher ability to transfer electrons compared with $\text{SiO}_x/\text{N-C}$ (Figure 6g,h).^[60,61]

The enhanced performances were attributed to the reasons: 1) Fe-N-C frameworks efficiently prevented the accumulation of SiO_x NPs and improved the electrochemical activity of SiO_x ; 2) Fe-N-C could both increase the conductivity and effectively alleviate the volume fluctuations caused by nano- SiO_x upon cycling; 3) Fe single atoms with catalytic attribute promoted the dissociation of Li_xSi phase and enhanced its electrochemical reversibility.

3. Conclusion

In summary, a simple electrospray-carbonization strategy for obtaining $\text{SiO}_x/\text{Fe-N-C}$ materials was developed. Atomically dispersed Fe sites embedded within spherical N-C frameworks was used as a good dispersion medium of SiO_x NPs. It was noted that Fe single atoms as the main existence form in $\text{SiO}_x/\text{Fe-N-C}$ were indeed proved by the HAADF-STEM and XAFS results. According to the experimental and DFT results, the presence of Fe-N-C frameworks not only boosted the conductivity, accommodated the volume changes of SiO_x , but also promoted the reversibility of Li_xSi , resulting in significantly improved electrochemical performance of $\text{SiO}_x/\text{Fe-N-C}$. Additionally, its lithium storage mechanism was also proved by the in situ XRD results. Finally, this work presented an efficient strategy to rationally fabricate metal single atoms/clusters decorating carbon/nano- SiO_x composite anodes for high-performance LIBs, which was also expected for other energy storage and conversion applications.

Supporting Information

Supporting Information is available from the Wiley Online Library or from the author.

Acknowledgements

X.G. and H.X. contributed equally to this work. This work was supported by the National Natural Science Foundation of China (U1904215), Natural Science Foundation of Jiangsu Province (BK20200044), Changjiang scholars program of the Ministry of Education (Q2018270), and China Postdoctoral Science Foundation (2022M722686). The authors also acknowledge the Priority Academic Program Development of Jiangsu Higher Education Institutions.

Conflict of Interest

The authors declare no conflict of interest.

Data Availability Statement

The data that support the findings of this study are available from the corresponding author upon reasonable request.

Keywords

atomically dispersed iron sites, catalytic attribute, Li-ion-battery anodes, nitrogen-doped carbon frameworks, silicon suboxide

Received: October 19, 2022

Revised: November 16, 2022

Published online: December 5, 2022

- [1] B. Chen, T. Wang, S. Zhao, J. Tan, N. Zhao, S. P. Jiang, Q. Zhang, G. Zhou, H. M. Cheng, *Adv. Mater.* **2021**, *33*, 2007090.
- [2] C. C. Hou, L. Zou, L. Sun, K. Zhang, Z. Liu, Y. Li, C. Li, R. Zou, J. Yu, Q. Xu, *Angew. Chem., Int. Ed.* **2020**, *59*, 7384.
- [3] Y. Li, S. Lin, D. Wang, T. Gao, J. Song, P. Zhou, Z. Xu, Z. Yang, N. Xiao, S. Guo, *Adv. Mater.* **2020**, *32*, 1906722.
- [4] Y. Zhang, P. Li, C. Zhao, G. Zhou, F. Zhou, Q. Zhang, C. Su, Y. Wu, *Sci. Bull.* **2022**, *67*, 1679.
- [5] Y. Wu, C. Ye, L. Yu, Y. Liu, J. Huang, J. Bi, L. Xue, J. Sun, J. Yang, W. Zhang, X. Wang, P. Xiong, J. Zhu, *Energy Storage Mater.* **2022**, *45*, 805.
- [6] R. Zhao, Z. Liang, R. Zou, Q. Xu, *Joule* **2018**, *2*, 2235.
- [7] H. Ye, Y. Li, *InfoMat* **2022**, *4*, e12291.
- [8] R. Xiao, T. Yu, S. Yang, K. Chen, Z. Li, Z. Liu, T. Hu, G. Hu, J. Li, H. M. Cheng, Z. Sun, F. Li, *Energy Storage Mater.* **2022**, *51*, 890.
- [9] X. Guo, G. Zhang, Q. Li, H. Xue, H. Pang, *Energy Storage Mater.* **2018**, *15*, 171.
- [10] H. Yuan, M. Wu, J. Zheng, Z. G. Chen, W. Zhang, J. Luo, C. Jin, O. Sheng, C. Liang, Y. Gan, Y. Xia, J. Zhang, H. Huang, Y. Liu, J. Nai, X. Tao, *Adv. Funct. Mater.* **2019**, *29*, 1809051.
- [11] G. Hu, R. Yu, Z. Liu, Q. Yu, Y. Zhang, Q. Chen, J. Wu, L. Zhou, L. Mai, *ACS Appl. Mater. Interfaces* **2021**, *13*, 3991.
- [12] X. D. Li, Y. M. Zhao, Y. F. Tian, Z. Y. Lu, M. Fan, X. S. Zhang, H. Tian, Q. Xu, H. L. Li, Y. G. Guo, *ACS Appl. Mater. Interfaces* **2022**, *14*, 27854.
- [13] H. Li, H. Li, Z. Yang, L. Yang, J. Gong, Y. Liu, G. Wang, Z. Zheng, B. Zhong, Y. Song, Y. Zhong, Z. Wu, X. Guo, *Small* **2021**, *17*, 2102641.
- [14] Z. Sun, F. Xin, C. Cao, C. Zhao, C. Shen, W. Q. Han, *Nanoscale* **2015**, *7*, 20426.

- [15] X. Guo, Y. Z. Zhang, F. Zhang, Q. Li, D. H. Anjum, H. Liang, Y. Liu, C. S. Liu, H. N. Alshareef, H. Pang, *J. Mater. Chem. A* **2019**, *7*, 15969.
- [16] H. Tian, H. Tian, W. Yang, F. Zhang, W. Yang, Q. Zhang, Y. Wang, J. Liu, S. R. P. Silva, H. Liu, G. Wang, *Adv. Funct. Mater.* **2021**, *31*, 2101796.
- [17] J. Xie, L. Sun, Y. Liu, X. Xi, R. Chen, Z. Jin, *Nano Res.* **2022**, *15*, 395.
- [18] W. Li, L. Zeng, Y. Wu, Y. Yu, *Sci. China Mater.* **2016**, *59*, 287.
- [19] Y. Jiang, C. Li, R. Yu, Y. Wang, L. Zhou, *ACS Appl. Mater. Interfaces* **2022**, *14*, 26775.
- [20] G. Li, J. Y. Li, F. S. Yue, Q. Xu, T. T. Zuo, Y. X. Yin, Y. G. Guo, *Nano Energy* **2019**, *60*, 485.
- [21] J. Liu, P. Kopold, P. A. van Aken, J. Maier, Y. Yu, *Angew. Chem., Int. Ed.* **2015**, *54*, 9632.
- [22] X. Guo, W. Li, Q. Zhang, Y. Liu, G. Yuan, P. Braunstein, H. Pang, *Chem. Eng. J.* **2022**, *432*, 134413.
- [23] D. Liu, Z. Han, J. Ma, L. Gao, J. Cai, L. Zhang, S. Cheng, J. Xie, *Chem. Eng. J.* **2021**, *420*, 129754.
- [24] T. Li, T. Lu, X. Li, L. Xu, Y. Zhang, Z. Tian, J. Yang, H. Pang, Y. Tang, J. Xue, *ACS Nano* **2021**, *15*, 20032.
- [25] L. Zhao, Y. Zhang, L.-B. Huang, X.-Z. Liu, Q.-H. Zhang, C. He, Z.-Y. Wu, L.-J. Zhang, J. Wu, W. Yang, L. Gu, J.-S. Hu, L.-J. Wan, *Nat. Commun.* **2019**, *10*, 1278.
- [26] Z. Ma, Y. Liu, J. Gautam, W. Liu, A. N. Chishti, J. Gu, G. Yang, Z. Wu, J. Xie, M. Chen, L. Ni, G. Diao, *Small* **2021**, *17*, 2102710.
- [27] Y. Zhang, S. Li, L. Cheng, Y. Li, X. Ren, P. Zhang, L. Sun, H. Y. Yang, *J. Mater. Chem. A* **2021**, *9*, 3388.
- [28] W. Liu, L. Zhang, X. Liu, X. Liu, X. Yang, S. Miao, W. Wang, A. Wang, T. Zhang, *J. Am. Chem. Soc.* **2017**, *139*, 10790.
- [29] T. Chen, J. Wu, Q. Zhang, X. Su, *J. Power Sources* **2017**, *363*, 126.
- [30] R. Xu, Y. Yao, H. Wang, Y. Yuan, J. Wang, H. Yang, Y. Jiang, P. Shi, X. Wu, Z. Peng, Z. Wu, J. Lu, Y. Yu, *Adv. Mater.* **2020**, *32*, 2003879.
- [31] M. Zhao, Y. Q. Peng, B. Q. Li, X. Q. Zhang, J. Q. Huang, *J. Energy Chem.* **2021**, *56*, 203.
- [32] P. Li, Z. Jin, Z. Fang, G. Yu, *Energy Environ. Sci.* **2021**, *14*, 3522.
- [33] S. An, G. Zhang, J. Liu, K. Li, G. Wan, Y. Liang, D. Ji, J. T. Miller, C. Song, W. Liu, Z. Liu, X. Guo, *Chin. J. Catal.* **2020**, *41*, 1198.
- [34] Y. Chen, Z. Li, Y. Zhu, D. Sun, X. Liu, L. Xu, Y. Tang, *Adv. Mater.* **2019**, *31*, 1806312.
- [35] S. Chen, X. Li, C.-W. Kao, T. Luo, K. Chen, J. Fu, C. Ma, H. Li, M. Li, T.-S. Chan, M. Liu, *Angew. Chem., Int. Ed.* **2022**, *61*, e202206233.
- [36] Y. Chen, S. Ji, Y. Wang, J. Dong, W. Chen, Z. Li, R. Shen, L. Zheng, Z. Zhuang, D. Wang, Y. Li, *Angew. Chem., Int. Ed.* **2017**, *56*, 6937.
- [37] X. Fu, P. Zamani, J.-Y. Choi, F. M. Hassan, G. Jiang, D. C. Higgins, Y. Zhang, M. A. Hoque, Z. Chen, *Adv. Mater.* **2017**, *29*, 1604456.
- [38] L. Zhou, K. Zhang, Z. Hu, Z. Tao, L. Mai, Y.-M. Kang, S.-L. Chou, J. Chen, *Adv. Energy Mater.* **2017**, *8*, 1701415.
- [39] M. Li, Y. Zeng, Y. Ren, C. Zeng, J. Gu, X. Feng, H. He, *J. Power Sources* **2015**, *288*, 53.
- [40] J. Zhao, H.-W. Lee, J. Sun, K. Yan, Y. Liu, W. Liu, Z. Lu, D. Lin, G. Zhou, Y. Cui, *Proc. Natl. Acad. Sci. USA* **2016**, *113*, 7408.
- [41] C. Guo, D. Wang, T. Liu, J. Zhu, X. Lang, *J. Mater. Chem. A* **2014**, *2*, 3521.
- [42] M. Gao, D. Wang, X. Zhang, H. Pan, Y. Liu, C. Liang, C. Shang, Z. Guo, *J. Mater. Chem. A* **2015**, *3*, 10767.
- [43] K. Wang, X. Zhu, Y. Hu, S. Qiu, L. Gu, C. Wang, P. Zuo, *Carbon* **2020**, *167*, 835.
- [44] Y. Cheng, B. Chen, M. Zhu, L. Chang, D. Zhang, C. Wang, S. Wang, L. Wang, *Appl. Mater. Today* **2021**, *25*, 101205.
- [45] X. Zhou, Z. Qi, Y. Jiang, P. Yan, J. Ding, H. Wang, H. Lu, D. Liu, K. Dong, Y. Tang, D. Sun, Z. Lei, *Electrochim. Acta* **2022**, *406*, 139805.
- [46] K. Zhang, D. Zhao, Z. Qian, X. Gu, J. Yang, Y. Qian, *Sci. China Mater.* **2022**, <https://doi.org/10.1007/s40843-022-2142-1>.
- [47] M. Du, P. Geng, C. Pei, X. Jiang, Y. Shan, W. Hu, L. Ni, H. Pang, *Angew. Chem., Int. Ed.* **2022**, *61*, e202209350.
- [48] W. Li, X. Guo, P. Geng, M. Du, Q. Jing, X. Chen, G. Zhang, H. Li, Q. Xu, P. Braunstein, H. Pang, *Adv. Mater.* **2021**, *33*, 2105163.
- [49] J. Tao, F. Wang, F. Han, Y. He, F. Zhang, J. Liu, *Electrochim. Acta* **2021**, *385*, 138431.
- [50] M. Han, Y. Mu, F. Yuan, J. Liang, T. Jiang, X. Bai, J. Yu, *J. Mater. Chem. A* **2020**, *8*, 3822.
- [51] T. Kang, J. Chen, Y. Cui, Z. Wang, H. Xu, Z. Ma, X. Zuo, X. Xiao, J. Nan, *ACS Appl. Mater. Interfaces* **2019**, *11*, 26038.
- [52] Z. Li, Q. He, L. He, P. Hu, W. Li, H. Yan, X. Peng, C. Huang, L. Mai, *J. Mater. Chem. A* **2017**, *5*, 4183.
- [53] C. Wang, J. Yan, T. Li, Z. Lv, X. Hou, Y. Tang, H. Zhang, Q. Zheng, X. Li, *Angew. Chem., Int. Ed.* **2021**, *60*, 25013.
- [54] F. Xi, Z. Zhang, Y. Hu, S. Li, W. Ma, X. Chen, X. Wan, C. M. Chong, B. Luo, L. Wang, *J. Hazard. Mater.* **2021**, *414*, 125480.
- [55] H. Yamamura, K. Nobuhara, S. Nakanishi, H. Iba, S. Okada, *J. Ceram. Soc. Jpn.* **2011**, *119*, 855.
- [56] J. Y. Kwon, J. H. Ryu, S. M. Oh, *Electrochim. Acta* **2010**, *55*, 8051.
- [57] Z. Liu, Q. Yu, Y. Zhao, R. He, M. Xu, S. Feng, S. Li, L. Zhou, L. Mai, *Chem. Soc. Rev.* **2019**, *48*, 285.
- [58] J. Heo, Y. Hwang, G. Doo, J. Jung, K. Shin, D. Koh, H. Kim, *Small* **2022**, *18*, 2201163.
- [59] H. Radinger, V. Trouillet, F. Bauer, F. Scheiba, *ACS Catal.* **2022**, *12*, 6007.
- [60] S. Zhang, Z.-Q. Huang, Y. Ma, W. Gao, J. Li, F. Cao, L. Li, C.-R. Chang, Y. Qu, *Nat. Commun.* **2017**, *8*, 15266.
- [61] F. Wang, Q. Ding, J. Ding, Y. Bai, H. Bai, W. Fan, *Chem. Eng. J.* **2022**, *450*, 138260.